

## PET Imaging of Tumor-Associated Macrophages with <sup>89</sup>Zr-labeled HDL Nanoparticles

Carlos Pérez-Medina,<sup>1,2,3</sup> Jun Tang,<sup>3,4</sup> Dalya Abdel-Atti,<sup>4</sup> Brandon Hogstad,<sup>5,6,7</sup> Miriam Merad,<sup>5,6,7</sup> Edward A. Fisher,<sup>8</sup> Zahi A. Fayad,<sup>3</sup> Jason S. Lewis,<sup>4,9</sup> Willem J.M. Mulder<sup>3,10,\*</sup> and Thomas Reiner<sup>4,9,\*</sup>

<sup>1</sup> Centro de Investigación en Red de Enfermedades Respiratorias, CIBERES, Madrid, Spain

<sup>2</sup> Centro Nacional de Investigaciones Cardiovasculares, CNIC, Madrid, Spain

<sup>3</sup> Translational and Molecular Imaging Institute, Icahn School of Medicine at Mount Sinai, New York, NY, USA

<sup>4</sup> Department of Radiology, Memorial Sloan Kettering Cancer Center, New York, NY, USA

<sup>5</sup> Department of Oncological Sciences, Icahn School of Medicine at Mount Sinai, New York, NY, USA

<sup>6</sup> The Tisch Cancer Institute, Icahn School of Medicine at Mount Sinai, New York, NY, USA

<sup>7</sup> Immunology Institute, Icahn School of Medicine at Mount Sinai, New York, NY, USA

<sup>8</sup> Leon H. Charney Division of Cardiology and Marc and Ruti Bell Program in Vascular Biology, New York University School of Medicine, New York, NY, USA

<sup>9</sup> Weill Cornell Medical College, New York, NY, USA

<sup>10</sup> Department of Vascular Medicine, Academic Medical Center of the University of Amsterdam, Amsterdam, The Netherlands

\*T. Reiner, PhD

Department of Radiology, Memorial Sloan-Kettering Cancer Center, 1275 York Avenue, New York, NY  
10065, USA

Phone: 646-888-3461 | Fax: 646-888-3059

Email: [reinert@mskcc.org](mailto:reinert@mskcc.org)

\*W.J.M. Mulder, PhD

Translational and Molecular Imaging Institute, Icahn School of Medicine at Mount Sinai, One Gustave  
L. Levy Place, Box 1234, New York, NY 10029, USA

Phone: 212-824-8910 | Fax: 646-537-9589

Email: [willem.mulder@mssm.edu](mailto:willem.mulder@mssm.edu)

C. Pérez-Medina, PhD (Postdoctoral Research Associate)

Translational and Molecular Imaging Institute, Icahn School of Medicine at Mount Sinai, 1470 Madison  
Avenue, New York, NY 10029

Phone: 212-824-8466 | Fax: 646-537-9589

Email: [carlos.perez-medina@mountsinai.org](mailto:carlos.perez-medina@mountsinai.org)

Financial Support: The authors thank the NIH (K25 EB016673 for T.R.), the Brain Tumor Center of Memorial Sloan-Kettering Cancer (for T.R.) as well as the Nanotechnology Center for Molecular Imaging and Nanotechnology (for T.R.) for their generous funding, and the CNIC Cardiolmage program (for C.P.M.). NIH grants R01 HL118440 (W.J.M.M.), R01 HL125703 (W.J.M.M.), R01 CA155432 (W.J.M.M.), NWO Vidi 91713324 (W.J.M.M.),

Word Count: 4700

Short running foot line: Tumor-Associated Macrophage Imaging with <sup>89</sup>Zr-HDL

## ABSTRACT

Tumor-associated macrophages (TAMs) are increasingly investigated in cancer immunology, and are considered a promising target for better and tailored treatment of malignant growth. Although TAMs also have high diagnostic and prognostic value, TAM imaging still remains largely unexplored. Here, we describe the development of reconstituted high-density lipoprotein (rHDL)-facilitated TAM positron emission tomography (PET) imaging in a breast cancer model.

**Methods:** Radiolabeled rHDL nanoparticles incorporating the long-lived positron-emitting nuclide  $^{89}\text{Zr}$  were developed using two different approaches. The nanoparticles were composed of phospholipids and apolipoprotein A-I (ApoA-I) in a 2.5:1 weight ratio.  $^{89}\text{Zr}$  was complexed with DFO, conjugated to either a phospholipid or ApoA-I protein to generate  $^{89}\text{Zr}$ -PL-HDL and  $^{89}\text{Zr}$ -AI-HDL, respectively. In vivo evaluation was carried out in an orthotopic mouse model of breast cancer and included pharmacokinetic analysis, biodistribution studies, and PET imaging. Ex vivo histological analysis of tumor tissues to assess regional distribution of  $^{89}\text{Zr}$  radioactivity was also performed. Fluorescent analogs of the radiolabeled agents were used to determine cell-targeting specificity using flow cytometry.

**Results:** The phospholipid- and apoA-I-labeled rHDL were produced at  $79 \pm 13$  % (n=6) and  $94 \pm 6$  % (n=6) radiochemical yield, respectively, with excellent radiochemical purity ( $> 99$  %). Intravenous administration of both probes resulted in high tumor radioactivity accumulation ( $16.5 \pm 2.8$  and  $8.6 \pm 1.3$  %ID/g for ApoA-I- and phospholipid-labeled rHDL, respectively) at 24 hours post injection. Histological analysis showed good co-localization of radioactivity with TAM-rich areas in tumor sections. Flow cytometry revealed high specificity of rHDL for TAMs, which had the highest uptake per cell (6.8-fold higher than tumor cells for both DiO@Zr-PL-HDL and DiO@Zr-AI-HDL) and accounted for 40.7 % and 39.5% of the total cellular DiO@Zr-PL-HDL and DiO@Zr-AI-HDL in tumors, respectively.

**Conclusions:** We have developed  $^{89}\text{Zr}$ -labeled TAM imaging agents based on the natural nanoparticle rHDL. In an orthotopic mouse model of breast cancer, we have demonstrated their specificity for macrophages, a result that was corroborated by flow cytometry. Quantitative macrophage PET imaging with our  $^{89}\text{Zr}$ -rHDL imaging agents could be valuable for non-invasive monitoring of TAM immunology and targeted treatment.

**KEYWORDS:** Tumor-associated macrophages,  $^{89}\text{Zr}$ , PET, high-density lipoprotein, breast cancer

## INTRODUCTION

Tumor-associated macrophage (TAM) immunology has become an active research field in recent years (1,2). Their complex role in carcinogenesis generally leads to disease progression in most cancers (3), which share some similar pathological mechanisms and, often, high TAM burden has been associated with poor prognosis (4). During cancer progression, circulating monocytes and macrophages are recruited to tumors, where they differentiate under the influence of a milieu of growth factors and cytokines (5). In this process, TAMs themselves become critical modulators of the tumor microenvironment, as they foster tumor growth (6), immune suppression, metastasis (7) and chemoresistance (1) by generating tumor-promoting conditions. TAMs' significant implication in modulating the immune system response to tumor growth has lead to various TAM-targeting therapies (8), some of which are being evaluated in the clinic (2,9,10).

For these reasons, specific and quantifiable TAM imaging agents are critical to evaluate the efficacy of TAM-targeting therapies and to facilitate prognosis of TAM-driven cancers. In fact, imaging of macrophages as key mediators of the inflammatory response is already an active area of research. Several nanoparticulate materials have been studied as such imaging agents (11). Among others, several iron oxide-based MRI probes have been applied (12,13), as well as  $^{64}\text{Cu}$ -labeled/mannose-functionalized liposomes (14), and nanobodies (15). Still, despite these efforts, clinical imaging of TAMs remains largely unexplored.

High-density lipoprotein (HDL) is a natural nanoparticle that has been exploited for magnetic resonance molecular imaging of the atherosclerotic plaque, and its specificity for macrophages has been established (16). Furthermore, in two recent studies, we have demonstrated its ability to deliver an anti-inflammatory drug to macrophages in atherosclerotic plaques with great specificity (17,18). To enable HDL's use for quantitative PET imaging of TAMs, we here present the design and synthesis of two different  $^{89}\text{Zr}$ -modified reconstituted HDL (rHDL) nanotracers, and their in vivo evaluation in an orthotopic mouse model of breast cancer. Specifically, we labeled either its protein component (apoA-I) or its phospholipid load, and examined the agent's TAM targeting using in vivo PET imaging and ex vivo analyses, including immunohistochemistry. Additionally, we prepared two fluorescent analogs of our radiolabeled  $^{89}\text{Zr}$ -rHDL nanotracers to allow us to gain insight into their cellular targets by flow cytometry.

## **MATERIALS AND METHODS**

A detailed description of the preparation of reconstituted HDL nanoparticles, their radiolabeling, as well as of all in vitro, in vivo and ex vivo experiments can be found in the Supplemental Data. All animal experiments were done in accordance with protocols approved by the Institutional Animal Care and Use Committee of MSKCC and followed National Institutes of Health guidelines for animal welfare.

## RESULTS

### Preparation of rHDL nanoparticles and radiolabeling with $^{89}\text{Zr}$ .

Reconstituted HDL (rHDL, Figure 1A) nanoparticles were prepared by mixing DMPC (dimyristoylphosphatidylcholine) vesicles with apoA-I. This resulted in discoidal particles with a mean hydrodynamic diameter of  $8.7 \pm 0.9$  nm ( $n=6$ ), as measured by DLS. The labeling of rHDL nanoparticles with  $^{89}\text{Zr}$  required prior modification of its components with the chelator DFO. Conjugation of DFO to apoA-I was achieved via reaction of its lysine amino groups with DFO-*p*-NCS on preformed rHDL particles. The resulting DFO-ApoA-I@rHDL had a diameter of  $8.9 \pm 1.1$  nm ( $n=5$ ). In order to label the phospholipid cargo, we incorporated the phospholipid chelator DSPE-DFO in the formulation at the expense of DMPC. Thus, we obtained 1 % DSPE-DFO@rHDL with a mean diameter of  $8.6 \pm 1.3$  nm ( $n=5$ ). The retention time of the two modified nanoparticles on size exclusion chromatography was identical and the same as unmodified rHDL, which corresponds to a species of estimated molecular weight (MW) of 150 kDa. Transmission electron microscopy images showed that both modified rHDL nanoparticles retained the discoidal shape (figure 1B). Radiolabeling of both DFO-ApoA-I@rHDL and 1 % DSPE-DFO@rHDL proceeded in high yield. ApoA-I-labeled rHDL ( $^{89}\text{Zr}$ -AI-HDL, figure 1A) was obtained in  $94 \pm 6$  % ( $n=6$ ) radiochemical yield (RCY); for phospholipid-labeled rHDL ( $^{89}\text{Zr}$ -PL-HDL, figure 1A), RCY was  $79 \pm 13$  % ( $n=6$ ). The composition, size and Zeta-potential of rHDL and the radiolabeled nanoparticles described in this study are shown in figure 1C. Radiochemical purity was greater than 99 % in both cases (figure 2A and 2B). As expected, the incubation of plain, unmodified rHDL particles with  $^{89}\text{Zr}$ -oxalate in the same conditions resulted in no detectable radiolabeling.

### In vitro serum stability of $^{89}\text{Zr}$ -labeled HDL nanotracers

In order to study label dynamics in vitro, the radiolabeled nanoparticles were incubated at 37 °C in fetal bovine serum. Analysis by size exclusion chromatography proved the dynamic nature of these nanoparticles. For  $^{89}\text{Zr}$ -AI-HDL, a new peak eluting at the same retention time as free apoA-I was detected. The ratio between  $^{89}\text{Zr}$ -AI-HDL and this species remained largely constant over time (table S1). Another species of MW > 300 kDa was observed at all time points.  $^{89}\text{Zr}$ -PL-HDL showed a similar dynamic behavior and a peak corresponding to larger particles of Mw > 300 kDa was also observed at all time points. Interestingly, activity directly associated with albumin was not detectable until 8 h and, in any case, the majority of it ( $63.3 \pm 1.5$  %) remained bound to HDL particles (figure 1C). The release of small radiolabeled species was detectable after 24 h for  $^{89}\text{Zr}$ -AI-HDL ( $5.5 \pm 0.7$  %,  $n=3$ ) and after 2 h for  $^{89}\text{Zr}$ -PL-HDL ( $3.3 \pm 0.6$  %,  $n=3$ , then reached  $11.7 \pm 6.4$  %,  $n = 3$ , after 24 h). This could be due to release of  $^{89}\text{Zr}$  from its DFO complex or a result of the degradation of the thiourea bond in the

presence of oxidizing chlorinated species (19) resulting in the detachment of the  $^{89}\text{Zr}$ -DFO unit. Collectively, however, these data suggest that both  $^{89}\text{Zr}$ -AI-HDL and  $^{89}\text{Zr}$ -PL-HDL are sufficiently stable to allow adequate in vivo evaluation.

### **Pharmacokinetics and biodistribution of $^{89}\text{Zr}$ -labeled HDL nanotracers**

Blood radioactivity clearance was markedly different, depending on whether the radiolabel was attached to Apo-AI or the phospholipid of rHDL. This indicates that the nanoparticle might not only be delivered passively but also actively distributed, governed by its natural biological function. The weighted half-life ( $t_{1/2}$ ) value measured for  $^{89}\text{Zr}$ -AI-HDL was 5.7 h, nearly 3 times longer than that shown by  $^{89}\text{Zr}$ -PL-HDL, whose  $t_{1/2}$  was 2.0 h (figure 3A). Tissue radioactivity distribution in female B6 mice bearing orthotopic 4T1-induced breast tumors was determined at 2 h, 24 h, and 48 h after administration. A selection of tissues is shown in figure 3B for both formulations, and a complete list of values can be found in the supplemental data (Tables S1 and S2). As expected from their blood half-lives, most of the radioactivity remains in blood at 2 h post-injection (p.i.). Significant accumulation was also observed in kidneys ( $16.4 \pm 2.1$  %ID/g [ $^{89}\text{Zr}$ -AI-HDL] and  $13.1 \pm 1.6$  ID/g [ $^{89}\text{Zr}$ -PL-HDL]), liver (significantly higher for  $^{89}\text{Zr}$ -PL-HDL [ $14.1 \pm 1.5$  %ID/g] than  $^{89}\text{Zr}$ -AI-HDL [ $7.51 \pm 2.21$  %ID/g]), and, to a lesser extent, spleen ( $5.0 \pm 1.2$  %ID/g and  $7.2 \pm 0.4$  %ID/g, respectively). Tumor uptake at this time point is below 5 % for both tracers. At 24 h p.i., blood activity levels had dropped to  $5.30 \pm 0.94$  and  $2.19 \pm 0.23$  %ID/g for  $^{89}\text{Zr}$ -AI-HDL and  $^{89}\text{Zr}$ -PL-HDL, respectively. A dramatic increase in tumor uptake can be observed for  $^{89}\text{Zr}$ -AI-HDL, reaching  $16.5 \pm 2.8$  %ID/g, whereas that of  $^{89}\text{Zr}$ -PL-HDL was  $8.6 \pm 1.3$  %ID/g. Kidney uptake was high for both nanotracers, but it was significantly higher for  $^{89}\text{Zr}$ -AI-HDL at  $21.2 \pm 1.9$  %ID/g. Of note, whole bone activity for  $^{89}\text{Zr}$ -PL-HDL went up to  $15.5 \pm 1.9$  %ID/g at this time point. Liver and spleen still retained a significant amount of activity. At 48 h p.i., liver, spleen, and kidney uptake are statistically identical for both radiolabeling approaches. Similarly, tumor uptake was  $12.3 \pm 4.5$  %ID/g for  $^{89}\text{Zr}$ -AI-HDL and  $12.0 \pm 4.7$  %ID/g for  $^{89}\text{Zr}$ -PL-HDL. The biggest discrepancy in biodistribution profiles at 48 h remained bone uptake, which was  $17.1 \pm 4.8$  %ID/g for  $^{89}\text{Zr}$ -PL-HDL and remained at  $2.70 \pm 0.62$  %ID/g for  $^{89}\text{Zr}$ -AI-HDL. We determined that  $3.6 \pm 1.1$  % of this uptake to originate from bone marrow, leaving  $96.4 \pm 1.1$  % associated with mineral bone, whereas for  $^{89}\text{Zr}$ -AI-HDL the fraction originating from bone marrow was  $27.8 \pm 4.1$  %.

### **In vivo imaging of $^{89}\text{Zr}$ -labeled HDL nanotracers**

PET imaging corroborated the observations obtained in ex vivo experiments (figure 4). The images collected at 24 h p.i. show strong liver, kidney, and tumor uptake for both nanotracers. Quantitative PET data (figure S1) was essentially in agreement with the biodistribution results. Using PET, tumor

uptake values were measured to be significantly higher for  $^{89}\text{Zr}$ -AI-HDL at  $16.7 \pm 1.6$  %ID/g ( $n=4$ ) than for  $^{89}\text{Zr}$ -PL-HDL ( $9.9 \pm 0.5$  %ID/g,  $n=4$ ). PET-quantified liver and kidney uptakes were higher for  $^{89}\text{Zr}$ -AI-HDL ( $20.8 \pm 2.9$  and  $29.3 \pm 11.5$  %ID/g [ $n=4$ ], respectively) than for  $^{89}\text{Zr}$ -PL-HDL ( $19.7 \pm 2.5$  and  $13.0 \pm 2.3$  %ID/g [ $n=4$ ]). PET-quantified blood activity concentrations, measured in the cardiac chambers, were significantly higher than those obtained from ex vivo experiments. At this time point, radioactivity in blood was  $7.9 \pm 1.6$  %ID/g ( $n=4$ ) for  $^{89}\text{Zr}$ -AI-HDL and  $4.7 \pm 1.5$  %ID/g ( $n=4$ ) for  $^{89}\text{Zr}$ -PL-HDL, and this difference was statistically significant.

Histological analysis of tumor sections collected at 24 h p.i. allowed us to establish regional distribution of both nanotracers (figure 5). Areas with high  $^{89}\text{Zr}$  deposition are highly vascularized, as shown by co-localization of CD31 and autoradiography (figures 5A and 5B). However, staining for Iba-1 (figure 5A and 5B) showed that particularly  $^{89}\text{Zr}$ -PL-HDL had also a high degree of co-localization to macrophage-rich areas (figure 5B).

### **Cellular distribution of $^{89}\text{Zr}$ -labeled HDL nanotracers**

The intercellular distribution of the  $^{89}\text{Zr}$ -labeled rHDL probes was determined by flow cytometry with their respective non-radioactive analogs Zr-AI-HDL and Zr-PL-HDL. Both were labeled with a fluorescent tag (DiO), using a previously reported procedure (17,18). Using size exclusion chromatography, the labeled nanoparticles DiO@Zr-AI-HDL and DiO@Zr-PL-HDL had the same retention time as their radiolabeled counterparts  $^{89}\text{Zr}$ -AI-HDL and  $^{89}\text{Zr}$ -PL-HDL, and as the unlabeled, plain rHDL. . We used a robust flow cytometry gating procedure to identify HDL levels in 7 relevant cell types, including TAMs, monocyte-derived cells, monocytes, dendritic cells (DC), T cells, endothelial cells (EC), and tumor cells (figure S1). We found the highest HDL uptake by TAMs, whose HDL levels were 3.5-fold (DiO@Zr-AI-HDL,  $P < 0.01$ ) and 4.1-fold (DiO@Zr-PL-HDL,  $P < 0.01$ ) higher than monocyte-derived cells; 19.0-fold ( $P < 0.01$ ) and 29.1-fold ( $P < 0.01$ ) higher than monocytes; 5.9-fold ( $P < 0.001$ ) and 6.5-fold ( $P < 0.001$ ) higher than dendritic cells ( $P < 0.05$ ); 124.2-fold ( $P < 0.01$ ) and 164.8-fold ( $P < 0.01$ ) higher than T cells; 6.3- ( $P < 0.01$ ) and 4.9-fold ( $P < 0.001$ ) higher than endothelial cells; and 6.8- ( $P < 0.01$ ) and 6.8-fold ( $P < 0.001$ ) higher than tumor cells (Figure 6). In this tumor model, TAMs accounted for  $7.0 \pm 4.4\%$  of total live cells but made up  $40.7 \pm 12.9\%$  (DiO@Zr-PL-HDL) and  $39.5 \pm 4.1\%$  (DiO@Zr-AI-HDL) of total intracellular HDL in all live cells. Using fluorescent, unmodified rHDL (DiO@rHDL), we found a strikingly similar cell targeting pattern to the two Zr-labeled fluorescent HDL formulations (figure S3), suggesting that Zr modification totally preserves the intrinsic TAM-targeting ability of rHDL. These data compellingly show that HDL not only efficiently accumulated in tumors but also specifically targeted TAMs.



## DISCUSSION

The aim of this study was to design a radiolabeled HDL-based nanoparticle to selectively target TAMs, capitalizing on HDL's biological function (20) rather than passive accumulation (via the EPR effect) (11) or hijacking a biomarker for targeted imaging (15). For this, we explored two different HDL labeling approaches: 1) attachment of the radiolabel to ApoA-I, the main apolipoprotein component of HDL; 2) radiolabeling of the phospholipid load of the particle. We chose  $^{89}\text{Zr}$  as the radioisotope as its physical half-life (78.2 h) matches the long biological half-life of HDL.

Both radiolabeling approaches required different DFO-modified building blocks. The first one was synthesized by conjugation of DFO to ApoA-I via reaction of the reconstituted HDL particles with DFO-*p*-NCS. The second one, the phospholipid-based chelator DSPE-DFO, was prepared as recently described by us (21). These modifications had no measurable effect on the size compared to plain rHDL (figure 1C). In both cases, the radiolabeling of the modified precursors resulted in the permanent association of the radioisotope to a particle fraction of an estimated molecular weight of 150 kDa. This molecular weight is in concordance with the expected molecular weight of discoidal HDL (22).

Biological evaluation was carried out in mice and provided insight into the nanoparticles' pharmacokinetics. The blood residence time differences likely reflect the different behavior of both components in natural HDL. The protein-labeled  $^{89}\text{Zr}$ -AI-HDL showed a significantly longer blood half-life (5.7 h) as opposed to the 2.0 h half-life observed for  $^{89}\text{Zr}$ -PL-HDL. It is well known that phospholipids transported by HDL exchange with other lipoproteins (23) before they are ultimately cleared from circulation when delivered to their targets. On the other hand, the net internalization and catabolic rate of apoA-I are very low, thus lengthening its circulation time, compared to the phospholipid-labeled nanoparticle (24). As a result, the  $^{89}\text{Zr}$ -AI-HDL-associated radioactivity half-life seems to match the slow turnover of HDL in the organism.

The breast cancer cell line 4T1 was chosen as a relevant breast cancer model to evaluate TAM targeting, since high TAM concentrations in tumors are associated with poor prognosis in this type of cancer (2). Acute radioactivity distribution in tissues in tumor-bearing mice provided similar blood-clearance profiles to the ones observed in blood half-life experiments. By 48 h p.i., less than 1 %ID/g remained in circulation ( $0.98 \pm 0.25$  vs  $0.49 \pm 0.06$  %ID/g for  $^{89}\text{Zr}$ -AI-HDL and  $^{89}\text{Zr}$ -PL-HDL, respectively). The high accumulation of radioactivity observed in the kidney, especially for  $^{89}\text{Zr}$ -AI-HDL, is in agreement with previous animal studies (25,26). Kidneys play an important role in apoA-I catabolism, probably via the proximal renal tubules, where it is taken up and degraded (27). ApoA-I is thus filtered through the glomerular basement membranes, followed by proximal tubule uptake, which

enables endocytosis of HDL proteins (28). In fact, a higher glomerular filtration rate is associated with low HDL and apoA-I levels in humans (29).

Tumor uptake was high for both formulations, peaking at  $16.5 \pm 2.8$  %ID/g at 24 h p.i. for  $^{89}\text{Zr}$ -AI-HDL, and  $12.0 \pm 4.7$  %ID/g at 48 h p.i. for  $^{89}\text{Zr}$ -PL-HDL. High accumulation of radioactivity in the bones of mice injected with  $^{89}\text{Zr}$ -PL-HDL was observed. For  $^{89}\text{Zr}$ -AI-HDL, whole bone uptake remained below 4 %ID/g at all time points, but a progressive increase is observed for  $^{89}\text{Zr}$ -PL-HDL, reaching 17 %ID/g at 48 h p.i. This was mainly associated with mineral bone for both probes, as less than 5 and 30 % of whole bone activity was taken up by bone marrow for  $^{89}\text{Zr}$ -PL-HDL and  $^{89}\text{Zr}$ -AI-HDL, respectively. The high accumulation of activity in the mineral component of the bone has been reported for other long-circulating  $^{89}\text{Zr}$ -labeled agents (30,31) and seems to be the result of liberation of  $^{89}\text{Zr}$  from its chelator (32). These data were largely in agreement with the respective PET imaging signatures. Intense signals were observed in kidneys and liver, as well as tumor, at 24 h p.i. (figure 4). Statistically significant differences were found for blood and tumor PET-derived uptake values between the two nanotracers. For  $^{89}\text{Zr}$ -PL-HDL, radioisotope uptake was also observed in the skeleton and joints mirroring ex vivo results. Most notably, ex vivo analysis of tumor sections allowed us to evaluate the nanoparticles' spatial and cell type distributions. Thus, both  $^{89}\text{Zr}$ -PL-HDL and  $^{89}\text{Zr}$ -AI-HDL seemed to accumulate in macrophage-rich regions, as evidenced by the co-localization of radioactivity to Iba-1 positive areas (figure 5).

Since histological analysis data are inherently qualitative of nature, we decided to further quantitatively elucidate cellular specificity by flow cytometry using fluorescently labeled analogs of the radiolabeled nanotracers modified with non-radioactive zirconium. Flow cytometry analysis of a comprehensive panel of biomarkers allowed us to differentiate the particles' preference for seven different cell types: TAMs, endothelial cells (EC), 4T1 tumor cells, monocyte-derived cells, monocytes, dendritic cells (DC), and T cells (figure 6). The variations in fluorescence intensities among the different cell types likely reflect how HDL nanoparticles interact with their targets. Similar to histological analysis, HDL preferentially targeted immune cells, particularly macrophages, followed by monocyte-derived cells and dendritic cells. Monocytes, T cells, endothelial cells, and tumor cells were only marginally targeted (figure 6C). Moreover, the targeting pattern of both Zr-labeled fluorescent analogs was very similar to that of the unmodified version (figure S2). These results, in conjunction with those observed on histological analysis, compellingly indicate that Zr-modified rHDL nanoparticles retain their biological function and that they target macrophages with high specificity.

## CONCLUSION

We have developed two high-yielding radiolabeling strategies to generate  $^{89}\text{Zr}$ -HDL nanoparticles and compared them in extensive studies. PET imaging allowed non-invasive visualization of the nanotracers' high accumulation in tumors, and ex vivo histological and flow cytometry analyses confirmed TAMs as their main target. The development of quantifiable macrophage imaging agents can meet important scientific and clinical needs, which include more accurate diagnoses, prognoses, and improved treatment monitoring. We therefore believe that our imaging agents could ultimately be of high value for non-invasive in vivo evaluation of TAM burden, not only in preclinical but also in clinical settings.

*Conflict of Interest:* The authors declare no competing financial interest.

## ACKNOWLEDGMENTS

The authors thank the Small Animal Imaging Core, the Radiochemistry and Molecular Imaging Probes Core and the Molecular Cytology Core at Memorial Sloan Kettering Cancer Center as well as the flow cytometry facility of The Tisch Cancer Institute of Icahn School of Medicine at Mount Sinai for support. The authors thank the NIH (K25 EB016673 for T.R.), the Brain Tumor Center of Memorial Sloan-Kettering Cancer (for T.R.) as well as the Nanotechnology Center for Molecular Imaging and Nanotechnology (for T.R.) for their generous funding, and the CNIC Cardiolmage program (for C.P.M.). We also wish to thank Christopher Irwin for his help with biodistribution experiments.

## REFERENCES

1. De Palma M, Lewis CE. Macrophage regulation of tumor responses to anticancer therapies. *Cancer Cell*. 2013;23:277-286.
2. Tang X. Tumor-associated macrophages as potential diagnostic and prognostic biomarkers in breast cancer. *Cancer Lett*. 2013;332:3-10.
3. Mantovani A, Locati M. Tumor-associated macrophages as a paradigm of macrophage plasticity, diversity, and polarization: lessons and open questions. *Arterioscler Thromb Vasc Biol*. 2013;33:1478-1483.
4. Chen Q, Zhang XH, Massague J. Macrophage binding to receptor VCAM-1 transmits survival signals in breast cancer cells that invade the lungs. *Cancer Cell*. 2011;20:538-549.
5. Franklin RA, Liao W, Sarkar A, Kim MV, Bivona MR, Liu K, Pamer EG et al. The cellular and molecular origin of tumor-associated macrophages. *Science*. 2014;344:921-925.
6. Coffelt SB, Hughes R, Lewis CE. Tumor-associated macrophages: effectors of angiogenesis and tumor progression. *Biochim Biophys Acta*. 2009;1796:11-18.
7. Condeelis J, Pollard JW. Macrophages: obligate partners for tumor cell migration, invasion, and metastasis. *Cell*. 2006;124:263-266.
8. Ries CH, Cannarile MA, Hoves S, Benz J, Wartha K, Runza V, Rey-Giraud F et al. Targeting tumor-associated macrophages with anti-CSF-1R antibody reveals a strategy for cancer therapy. *Cancer Cell*. 2014;25:846-859.
9. Noy R, Pollard JW. Tumor-associated macrophages: from mechanisms to therapy. *Immunity*. 2014;41:49-61.
10. Zhang QW, Liu L, Gong CY, Shi HS, Zeng YH, Wang XZ, Zhao YW et al. Prognostic significance of tumor-associated macrophages in solid tumor: a meta-analysis of the literature. *PLoS One*. 2012;7:e50946.

11. Weissleder R, Nahrendorf M, Pittet MJ. Imaging macrophages with nanoparticles. *Nat Mater.* 2014;13:125-138.
12. Daldrup-Link H, Coussens LM. MR imaging of tumor-associated macrophages. *Oncoimmunology.* 2012;1:507-509.
13. Leimgruber A, Berger C, Cortez-Retamozo V, Etzrodt M, Newton AP, Waterman P, Figueiredo JL et al. Behavior of endogenous tumor-associated macrophages assessed in vivo using a functionalized nanoparticle. *Neoplasia.* 2009;11:459-68, 2 p following 468.
14. Locke LW, Mayo MW, Yoo AD, Williams MB, Berr SS. PET imaging of tumor associated macrophages using mannose coated <sup>64</sup>Cu liposomes. *Biomaterials.* 2012;33:7785-7793.
15. Movahedi K, Schoonooghe S, Laoui D, Houbracken I, Waelput W, Breckpot K, Bouwens L et al. Nanobody-based targeting of the macrophage mannose receptor for effective in vivo imaging of tumor-associated macrophages. *Cancer Res.* 2012;72:4165-4177.
16. Skajaa T, Cormode DP, Falk E, Mulder WJ, Fisher EA, Fayad ZA. High-density lipoprotein-based contrast agents for multimodal imaging of atherosclerosis. *Arterioscler Thromb Vasc Biol.* 2010;30:169-176.
17. Duivenvoorden R, Tang J, Cormode DP, Mieszawska AJ, Izquierdo-Garcia D, Ozcan C, Otten MJ et al. A statin-loaded reconstituted high-density lipoprotein nanoparticle inhibits atherosclerotic plaque inflammation. *Nat Commun.* 2014;5:3065.
18. Tang J, Lobatto ME, Hassing S, van der Staay S, van Rijs SM, Calcagno C, Braza MS et al. Inhibiting macrophage proliferation suppresses atherosclerotic plaque inflammation. *Sci Adv.* 2015;1:e1400223.
19. Vosjan MJ, Perk LR, Visser GW, Budde M, Jurek P, Kiefer GE, van Dongen GA. Conjugation and radiolabeling of monoclonal antibodies with zirconium-89 for PET imaging using the bifunctional chelate p-isothiocyanatobenzyl-desferrioxamine. *Nat Protoc.* 2010;5:739-743.
20. Marcel YL, Ouimet M, Wang MD. Regulation of cholesterol efflux from macrophages. *Curr Opin Lipidol.* 2008;19:455-461.

21. Perez-Medina C, Abdel-Atti D, Zhang Y, Longo VA, Irwin CP, Binderup T, Ruiz-Cabello J et al. A modular labeling strategy for in vivo PET and near-infrared fluorescence imaging of nanoparticle tumor targeting. *J Nucl Med*. 2014;55:1706-1711.
22. Chen B, Ren X, Neville T, Jerome WG, Hoyt DW, Sparks D, Ren G et al. Apolipoprotein A-I tertiary structures determine stability and phospholipid-binding activity of discoidal high-density lipoprotein particles of different sizes. *Protein Sci*. 2009;18:921-935.
23. Illingworth DR, Portman OW. Exchange of phospholipids between low and high density lipoproteins of squirrel monkeys. *J Lipid Res*. 1972;13:220-227.
24. Marsh JB, Welty FK, Schaefer EJ. Stable isotope turnover of apolipoproteins of high-density lipoproteins in humans. *Curr Opin Lipidol*. 2000;11:261-266.
25. Glass CK, Pittman RC, Keller GA, Steinberg D. Tissue sites of degradation of apoprotein A-I in the rat. *J Biol Chem*. 1983;258:7161-7167.
26. Braschi S, Neville TA, Maugeais C, Ramsamy TA, Seymour R, Sparks DL. Role of the kidney in regulating the metabolism of HDL in rabbits: evidence that iodination alters the catabolism of apolipoprotein A-I by the kidney. *Biochemistry*. 2000;39:5441-5449.
27. Dallinga-Thie GM, Van 't Hooft FM, Van Tol A. Tissue sites of degradation of high density lipoprotein apolipoprotein A-IV in rats. *Arteriosclerosis*. 1986;6:277-284.
28. Hammad SM, Barth JL, Knaak C, Argraves WS. Megalin acts in concert with cubilin to mediate endocytosis of high density lipoproteins. *J Biol Chem*. 2000;275:12003-12008.
29. Krikken JA, Gansevoort RT, Dullaart RP. Lower HDL-C and apolipoprotein A-I are related to higher glomerular filtration rate in subjects without kidney disease. *J Lipid Res*. 2010;51:1982-1990.
30. Zeglis BM, Mohindra P, Weissmann GI, Divilov V, Hilderbrand SA, Weissleder R, Lewis JS. Modular strategy for the construction of radiometalated antibodies for positron emission tomography based on inverse electron demand Diels-Alder click chemistry. *Bioconjug Chem*. 2011;22:2048-2059.
31. Chang AJ, Desilva R, Jain S, Lears K, Rogers B, Lapi S. <sup>89</sup>Zr-Radiolabeled Trastuzumab Imaging in Orthotopic and Metastatic Breast Tumors. *Pharmaceuticals (Basel)*. 2012;5:79-93.

32. Abou DS, Ku T, Smith-Jones PM. In vivo biodistribution and accumulation of  $^{89}\text{Zr}$  in mice. *Nucl Med Biol.* 2011;38:675-681.

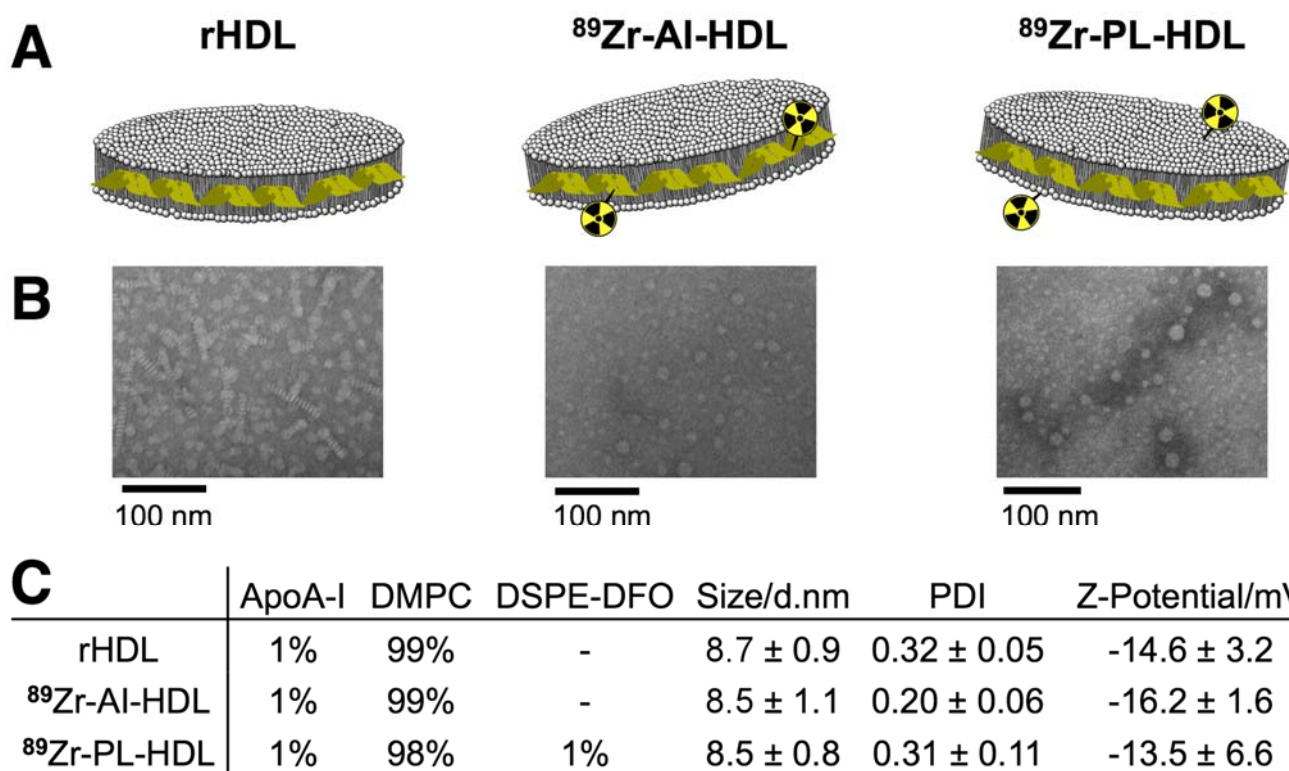


**Figure 1. Structure and composition of rHDL and <sup>89</sup>Zr-HDL nanotracers.** A) Schematic of rHDL (left), <sup>89</sup>Zr-AI-HDL (middle) and <sup>89</sup>Zr-PL-HDL (right). B) Transmission electron microscopy (TEM) images of rHDL (left), Zr-AI-HDL (middle) and Zr-PL-HDL (right). C) Composition (in mol %), size, polydispersity index (PDI) and surface charge of rHDL, <sup>89</sup>Zr-AI-HDL and <sup>89</sup>Zr-PL-HDL. Data are presented as mean ± SD (n ≥ 3).



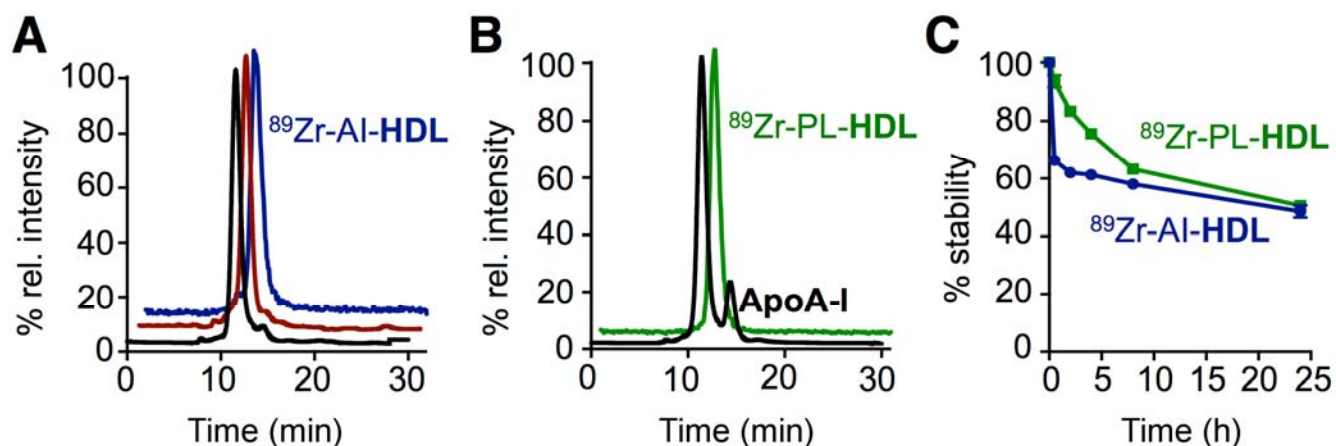


**Figure 2. Radiosynthesis and in vitro stability of  $^{89}\text{Zr}$ -HDL nanotracers.** Size exclusion chromatograms showing A) coelution of plain rHDL (black trace), DFO-ApoA-I@rHDL (red trace) and  $^{89}\text{Zr-AI-HDL}$  (blue, radioactive trace); and B) coelution of 1% DSPE-DFO@rHDL (black trace) and  $^{89}\text{Zr-PL-HDL}$  (green, radioactive trace). C) In vitro serum stability of  $^{89}\text{Zr}$ -HDL nanotracers at 37 °C.

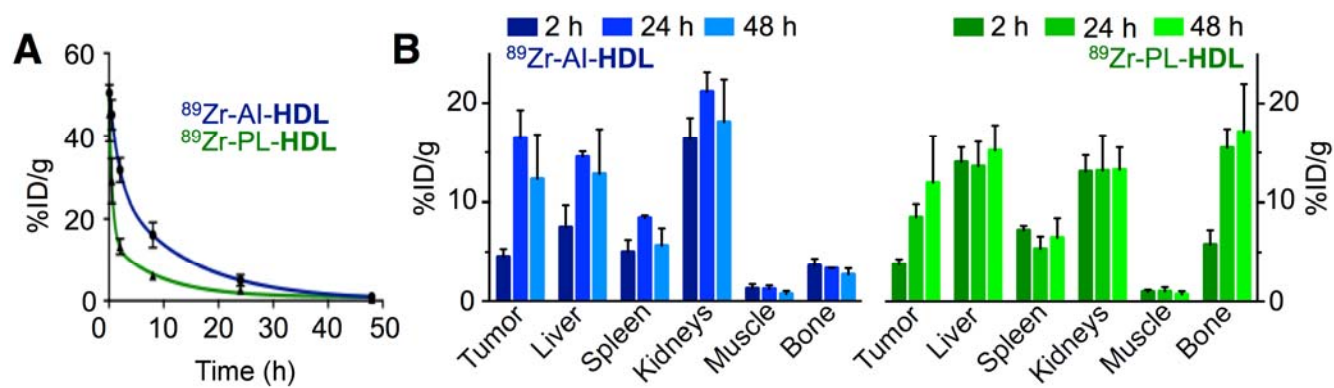


**Figure 3. Pharmacokinetics and biodistribution of  $^{89}\text{Zr}$ -HDL nanotracers.** A) Blood time-activity curve for  $^{89}\text{Zr}$ -AI-HDL and  $^{89}\text{Zr}$ -PL-HDL ( $n = 3$ ). B) Radioactivity distribution in selected tissues of  $^{89}\text{Zr}$ -AI-HDL (blue) and  $^{89}\text{Zr}$ -PL-HDL (green) in mice bearing orthotopic breast cancer tumors, expressed as %ID/g  $\pm$  SD ( $n \geq 3$ ).

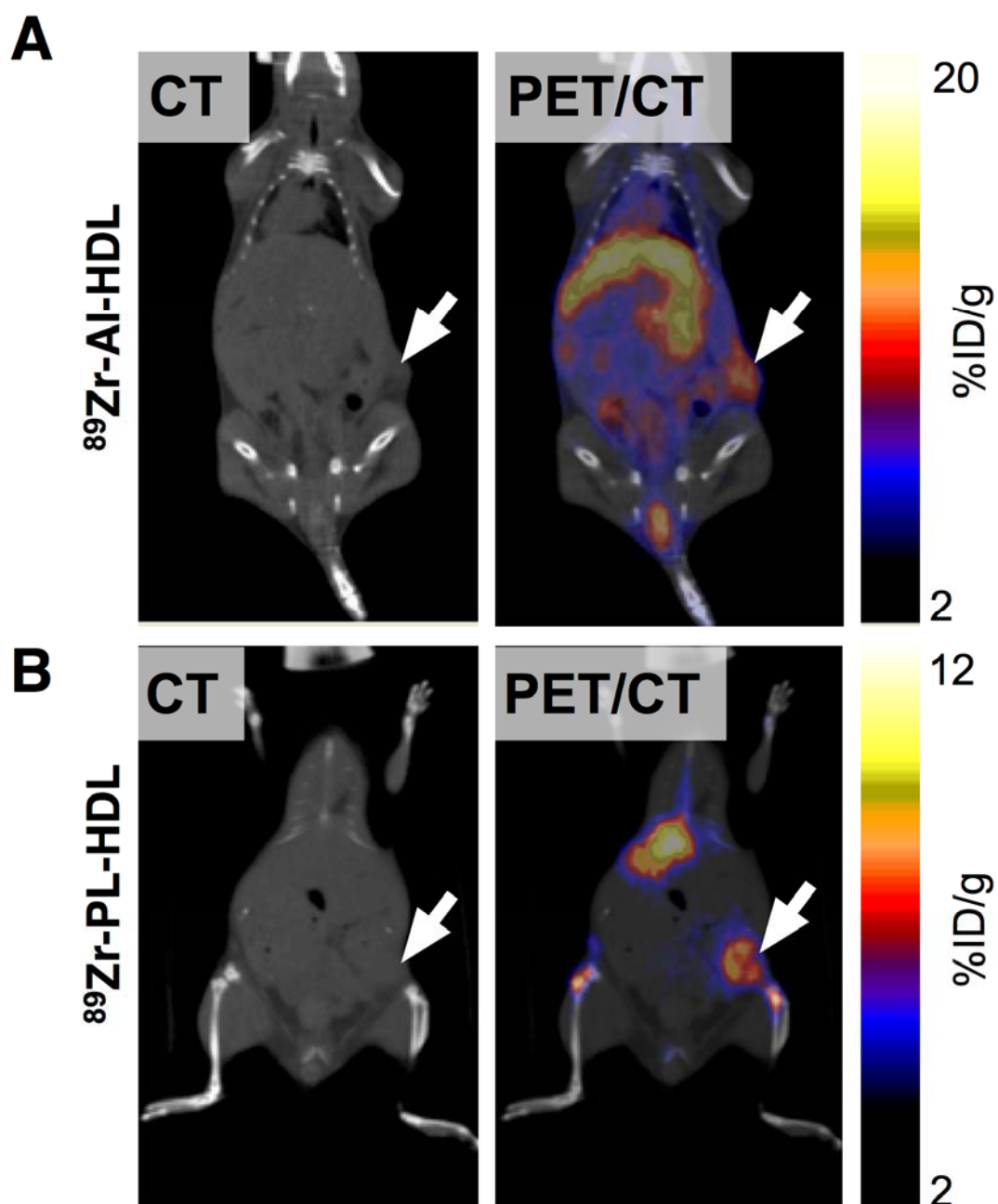


**Figure 4.** The accumulation of  $^{89}\text{Zr}$ -HDL nanotracers in tumor tissues can be visualized by in vivo PET imaging. CT (left) and PET/CT fusion (right) images of A)  $^{89}\text{Zr}$ -AI-HDL and B)  $^{89}\text{Zr}$ -PL-HDL obtained at 24 h post injection in mice bearing orthotopic 4T1 tumors (indicated by arrows).

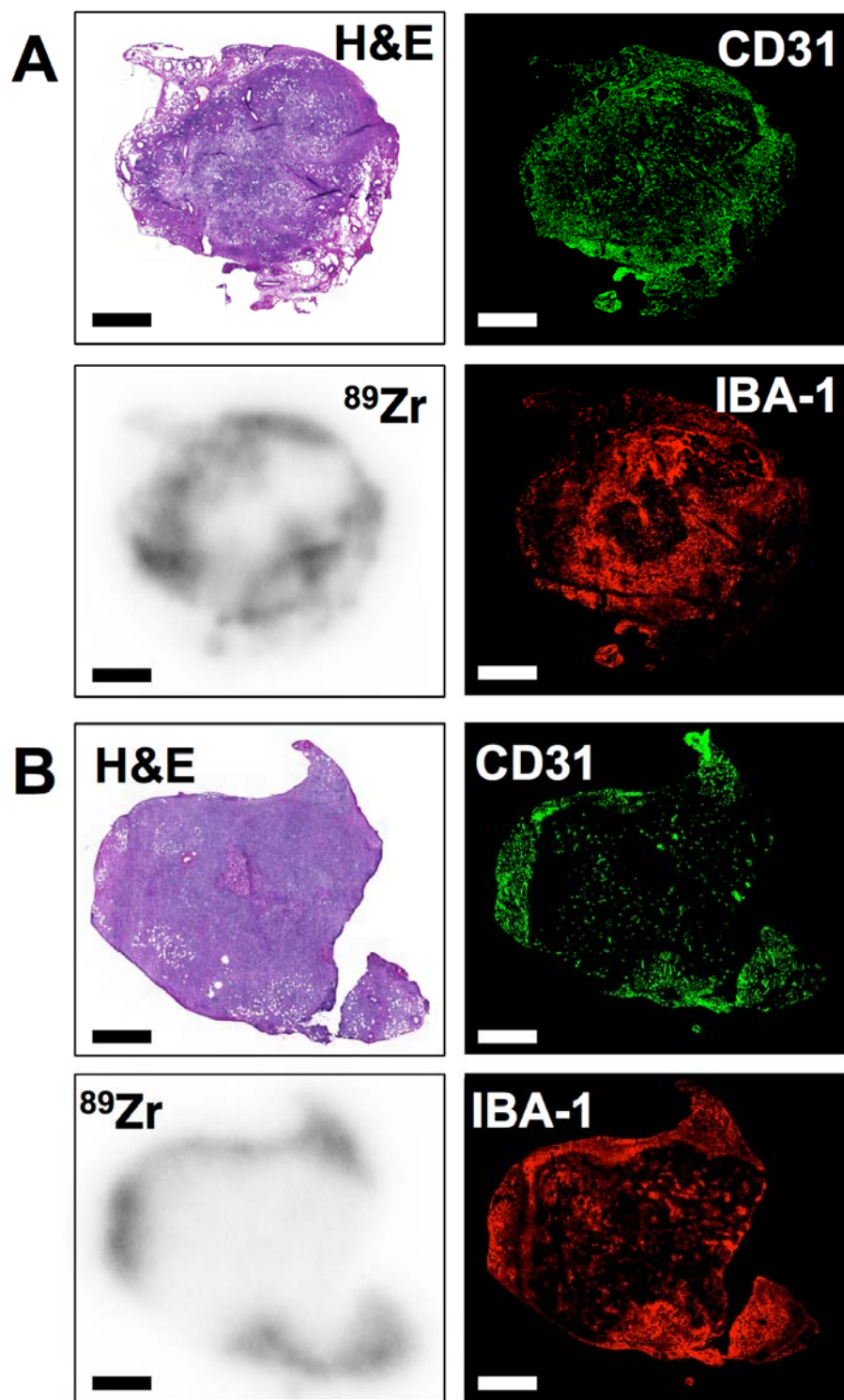


**Figure 5.  $^{89}\text{Zr}$ -HDL nanotracers accumulate in TAM-rich areas.** Ex vivo histological analysis of a tumor sections at 24 h after administration of HDL nanotracers, showing hematoxylin and eosin staining (top left), immunofluorescence for CD31 (top right) and IBA-1 (bottom right), and autoradiography (bottom left) for A)  $^{89}\text{Zr}$ -AI-HDL and B)  $^{89}\text{Zr}$ -PL-HDL. Scale bar = 2 mm.

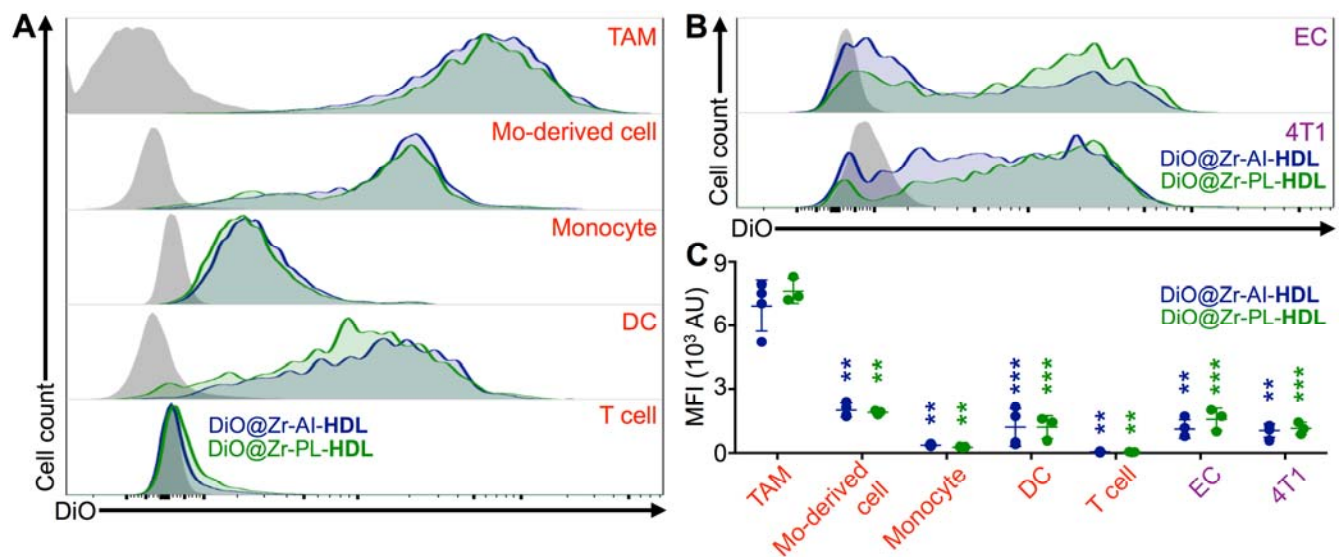


**Figure 6. Both DiO@Zr-PL-HDL and DiO@Zr-AI-HDL preferentially target tumor-associated macrophages.** 4T1-cell-induced orthotopic breast tumors were used to isolate single cells. A) Representative DiO levels in five immune cells, namely tumor-associated macrophages (TAM), monocyte-derived cells (Mo-derived cell), monocytes, dendritic cells (DC), and T cells. B) Representative DiO levels in endothelial cells (EC) and tumor cells (4T1). Cells from a PBS-injected mouse served as controls (grey histograms to the left). C) Quantification of DiO levels presented as mean fluorescence intensity (MFI). Importantly, no statistical significance was found when comparing the DiO levels of the same cell type from the two HDL formulations. Statistics was calculated with two-tailed Student's *t*-test with unequal variance by comparing to TAM from the same group. \*\*  $P < 0.01$ , \*\*\*  $P < 0.001$ .